

A Recursive Division Stochastic Strike-Slip Seismic Source Algorithm Using Insights from Laboratory Earthquakes

H. Siriki, A.J. Rosakis, & S. Krishnan

Division of Engineering and Applied Science, California Institute of Technology, USA -91106

H. S. Bhat

Institut de Physique du Globe de Paris, France

X. Lu

Intel Corporation, Phoenix, USA



SUMMARY:

There are a sparse number of credible source models available from past earthquakes and a stochastic source model generation algorithm thus becomes necessary for robust risk quantification using scenario earthquakes. We present an algorithm that combines the physics of fault rupture as imaged in laboratory earthquakes with stress estimates on the fault constrained by field observations to generate probability distributions of rise-time and rupture-speed for strike-slip earthquakes. The algorithm is validated through a statistical comparison of peak ground velocity at 636 sites in Southern California from synthetic ground motion histories simulated for 10 rupture scenarios using a stochastically generated source model against that generated using a kinematic source model from a finite source inversion. This model, selected from a set of 5 stochastically generated source models, produces ground shaking intensities in Southern California with a median that is closest to the median intensity of shaking from all 5 source models (and 10 rupture scenarios per model).

Keywords: seismic risk quantification, source model generation algorithm, laboratory earthquakes.

1. INTRODUCTION

Rupture-to-rafters simulations provide a holistic approach towards the safe design of structures. Generating stochastic seismic source models for these simulations is a crucial step, given the limited number of credible source models from historical earthquakes. The seismic source model is a mathematical representation of the earthquake rupture process. Two types of source models are used in earthquake physics: (i) “kinematic” models, which prescribe the spatial and temporal evolution of the rupture speed, the slip, and the slip velocity on the fault, inferred from seismic, geodetic, and geological observations; and (ii) “dynamic” models, which prescribe the fault prestress, fracture energy, and stress drop. An earthquake is nucleated at a point in the model by artificially increasing the pre-stress above the shear strength. The rupture process is then allowed to evolve dynamically as dictated by an assumed fault friction law. The development of dynamic source models is an active area of research in earthquake source physics (e.g., Schmedes et al. 2010). While dynamic source models may better characterize earthquake source physics, the theory is more complex and less mature when compared to kinematic source modeling (e.g., the state of stress in the earth and the fault friction law are not known; they are not as well-constrained as kinematic source parameters such as slip). Here, we represent an earthquake source using a kinematic model. Kinematic description of the source involves dividing the fault rupture plane(s) into a number of smaller sub-events. Each sub-event is characterized by three parameters: slip, rupture speed and slip velocity-time function. Brune (1970) proposed one of the earliest models for earthquake source representation, in which near and far-field displacement spectra are calculated from a fault dislocation model representation accelerated by effective stress. Significant progress has been made in kinematic source modeling since then with the help of data collected by modern seismic networks. We start with a brief description of existing and current approaches to prescribing the three source parameters for each sub-event.

1.1. Slip Distribution

Of the three source parameters, spatial variation of slip is perhaps the best understood parameter, partly due to the fact that surface slip in a finite source inversion of an earthquake can be constrained using geodetic observations. The power spectral density (PSD) of the two-dimensional slip distribution in these inversions typically decays with wave number according to a power law. On the basis of this observation, a PSD function, inferred from finite-source inversions of past earthquakes, could be inverted back to the spatial domain to produce a stochastic slip model (e.g., Somerville et al. 1999, Mai and Beroza 2002). It should be noted that inversions of only a limited number of large magnitude earthquakes were used in these studies to develop the PSD function (e.g., see Fig. 1.1). Moreover this approach anchors the sources to a specific value of power-spectral decay and may not capture the degree of variability perhaps inherent to seismic sources.

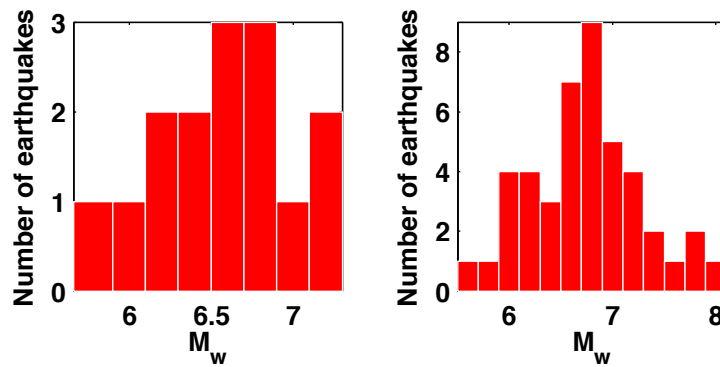


Figure 1.1. Histograms of magnitudes of past earthquakes considered by (left) Somerville et al. 1999 (right) Mai and Beroza 2002 for determining spectral properties of the distribution of slip on the fault. The source mechanisms of these earthquakes are not limited to strike-slip, but include reverse, thrust etc. Note the sparse number of large magnitude ($M_w \geq 7.0$) earthquakes included in either study.

An alternate approach, adopted here, is to generate spatial distributions of slip stochastically and accept or reject each model by comparing its spectral properties against that of finite-source inversions of past earthquakes. Our algorithm is based on a recursive division model in which the rupture area is divided recursively along length, until each daughter segment has a dimensional aspect ratio close to 1.0. Lognormal probability distributions are used to characterize mean slip on each daughter segment. The mean and standard deviation of the distribution depends upon the magnitude of its parent segment. Slip on each daughter segment is assigned a value equal to a single realization of the corresponding probability distribution, with the slip vector oriented along length (rake is 180° , pure strike slip fault). To introduce slip variation along depth, each (approximately square) daughter segment is subdivided into four segments using one subdivision along depth and one along length. The assignment of slip for this penultimate generation of daughter segments is based on the same method as the previous generations of daughter segments. Finally, these penultimate generation segments are subdivided along length and depth to the resolution needed for wave propagation simulations. Slips are assigned to this final generation of segments as realizations of the lognormal probability distribution corresponding to the magnitude of the corresponding parent segment from the penultimate generation. A filter is applied to smoothen the resulting slip distribution eliminating sharp spatial variations. Additionally at each step the mean slips are scaled linearly to that of the parent segment such that the net seismic moment M_0 is conserved. The resulting slip distribution is accepted if the average power spectra, along the length and the depth of the rupture, decay with wave number according to a power law with decay coefficient between 2.0 and 4.0. This is the range of values for the decay published in literature (e.g., Somerville et al. 1999, Mai and Beroza 2002).

1.2. Rupture Speed Distribution

The initiation time of slip at any given location along the rupture depends upon the rupture speed V_r . Rupture speed can have a significant effect on the character of the radiated seismic waves, the

resulting ground motion and the impact on the built environment. While rupture speeds have traditionally been assumed to be smaller than the Rayleigh wave speed, evidence from recent earthquakes such as 1999 M_w 7.6 Izmit (e.g., Bouchon et al 2002), 2001 M_w 7.8 Kunlun (e.g., Bouchon and Vallée 2003), and 2002 M_w 7.9 Denali (e.g., Frankel 2004) point to rupture speeds exceeding the shear wave speed. Based in part on this evidence, several new models have been developed with an underlying principle that rupture speed is correlated with slip on the fault (e.g., Liu et al. 2006, Aagaard et al. 2010). However, Schmedes et al. (2010) could not find evidence of such correlation in dynamic rupture models of 315 earthquakes. An alternative resource for gaining insights into the rupture process is a laboratory earthquake catalogue. Stable pulse-like ruptures have been realized in the laboratory under controlled conditions (e.g., Lu et al. 2010). Rupture speeds in the vicinity of $0.87V_s$ and $1.67V_s$ (V_s is the shear wave speed in the medium) have been measured for ruptures propagating at sub-Rayleigh and super-shear speeds, respectively. In our source representation, we assume that rupture initiates at a sub-Rayleigh speed of $0.87V_s$ and use estimates of pre-stress on the fault from geodetic, borehole and other observations catalogued in the World Stress Map project to assess whether conditions exist for rupture to transition to super-shear speeds as it progresses along the fault. If such conditions exist for any sub-event, we prescribe a rupture speed of $1.67V_s$ for the same.

1.3. Slip Velocity-Time Function

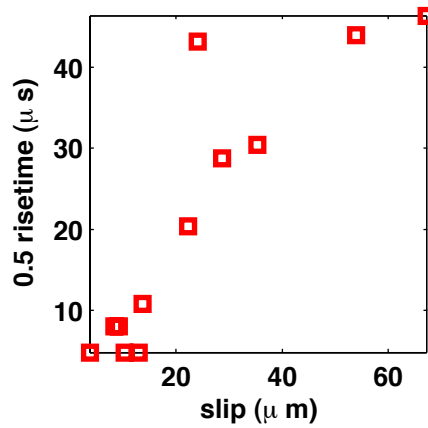


Figure 1.2. Rise-time vs slip as observed in laboratory earthquakes. The correlation between the two is in agreement with dynamic rupture studies conducted by Schmedes et al. 2010.

The slip velocity-time function describes the temporal evolution of slip during an earthquake and is characterized by slip magnitude, rise-time (time taken for slip to reach its maximum) and peak time (time taken to reach maximum slip velocity). Variation of slip velocity with time in a source model affects the frequency and amplitude characteristics of the resulting ground motions. It is defined either by a single function (single time window) or by a series of overlapping time-shifted functions (multiple time window). Given the lack of field observations that capture source physics, our only alternative is to use insights from laboratory earthquakes to constrain the slip velocity-time function. In the laboratory earthquakes generated by Lu et al. (2010), rise-time (measured in micro-seconds) is linearly correlated with slip (measured in micro-meters) as shown in Fig. 1.2. This is in agreement with dynamic rupture studies (e.g., Schmedes et al. 2010) and similar to Aagaard et al. (2010), where they postulate rise time being proportional to the square root of the slip. We fit a lognormal probability density function (PDF) to the slip to rise-time ratio measured in the laboratory earthquakes. Using a self-similarity assumption of the mean and variance of the slip to rise-time ratio at the laboratory scale being equivalent to that at the earth scale (i.e., $\left. \frac{D}{T_r} \right|_{earth} = \left. \frac{D}{T_r} \right|_{lab}$), we then assign independent realizations of this PDF as the slip to rise-time ratio for each rupture segment. A slip proportional rise-time (and slip velocity) is thus prescribed to each segment. It should be noted that Andrews and Barall (2011) make a comparable self-similar assumption, that the mean and variance of a PDF for ratio of initial shear stress to initial normal stress on the fault is scale independent.

2. METHODOLOGY

2.1. Slip (D)

For a given magnitude M_w , rupture area A is estimated using one of several existing magnitude-area relationships. Given the seismogenic depth d from field observations, the length of the rupture l can be determined. If d exceeds “ l ”, the rupture dimensions are recalculated assuming a square rupture area. Seismic moment M_0 and mean slip \bar{D} are estimated using:

$$M_0 = 10^{1.5 M_w + 10.7} = G A \bar{D} \quad (2.1)$$

where G is shear modulus of earth (~ 30 GPa). Shown in Fig. 2.1. is the standard deviation of lognormal PDFs of slip in finite-source inversions of 56 past strike-slip earthquakes (<http://www.seismo.ethz.ch/Events.html>) with magnitude M_w in the 6.0-8.0 range, plotted as a function of earthquake magnitude. A linear trend can be seen. We use a linear fit to this data to correlate the standard deviation of a lognormal PDF characterizing fault slip as a function of magnitude for use in our recursive division approach. In this approach, the rupture area is recursively subdivided along length into smaller segments, with each parent segment being subdivided into two daughter segments. This segmentation is continued until each segment on the fault attains a dimensional aspect ratio close to unity. Given the magnitude associated with the parent segment, the standard deviation of the lognormal PDF to be used for slip characterization of the daughter segment is determined using the linear relation of Fig. 2.1. Two independent realizations of this PDF are assigned as mean slip on the two daughter segments. They are scaled uniformly so that the sum of seismic moments of the daughter segments matches that of the parent segment. If parent segment M_w is less than 6.0 (lower magnitude limit in Fig. 2.1.), the standard deviation corresponding to M_w 6.0 is used.

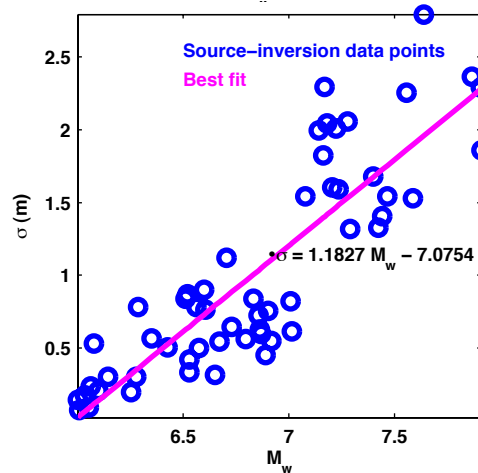


Figure 2.1. Standard deviation σ of lognormal probability density functions of slip in finite-source inversions of 56 past strike-slip earthquakes in the M_w 6.0-8.0 range. A linear trend between σ and M_w can be seen. The best least squares linear fit for the data is shown as well.

In the penultimate step, each resulting fault segment is divided into 4 daughter segments (two along length and depth alike) to introduce along-depth variation of slip. Mean slips are assigned to each as before. In the case of the San Andreas fault with a seismogenic depth of approximately 20 km., the area of the resulting fault segments ($\sim 10\text{km.} \times 10\text{km.}$) approximates that of an M_w 6.0 earthquake (consistent with the lower magnitude limit of the finite-source inversions used in Fig. 2.1.). Finally, each fault segment is discretized to the resolution required for wave propagation simulations. Slips are assigned as before. Note that the final division is done in one step and not recursively. A unit 2-D filter that is Gaussian along length and parabolic along depth is applied to smoothen the slip distribution. The dimensions of the filter are d & $\frac{3}{4}d$ along length and depth, respectively, chosen by a trial and

error process to prevent distortion of slip around fault area. The parabola has zero ordinate at the bottom of the filter and a maximum at two-thirds height ensuring that maximum moment release occurs within the upper portion of the fault (consistent with Fialko et al. 2005). One realization of a slip model generated from this algorithm is illustrated in Fig. 2.2. If the average of the PSDs of the slip in each segment layer along length and depth decays with increasing wave number as a power law with decay coefficient between 2.0 and 4.0 (Fig. 2.3), the slip distribution is accepted, else it is rejected.

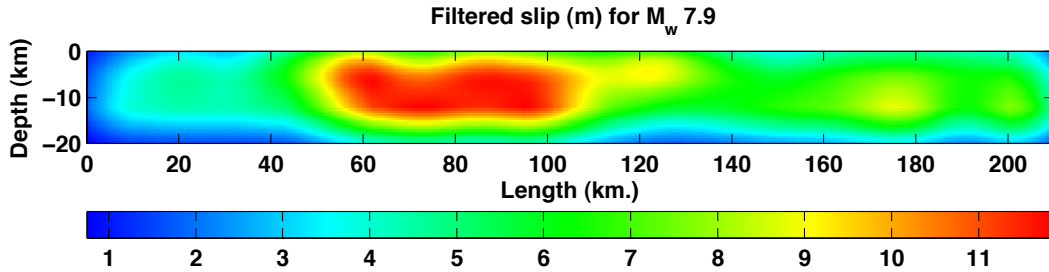


Figure 2.2. Stochastic slip realization for a $M_w 7.9$ earthquake generated using the recursive division algorithm.

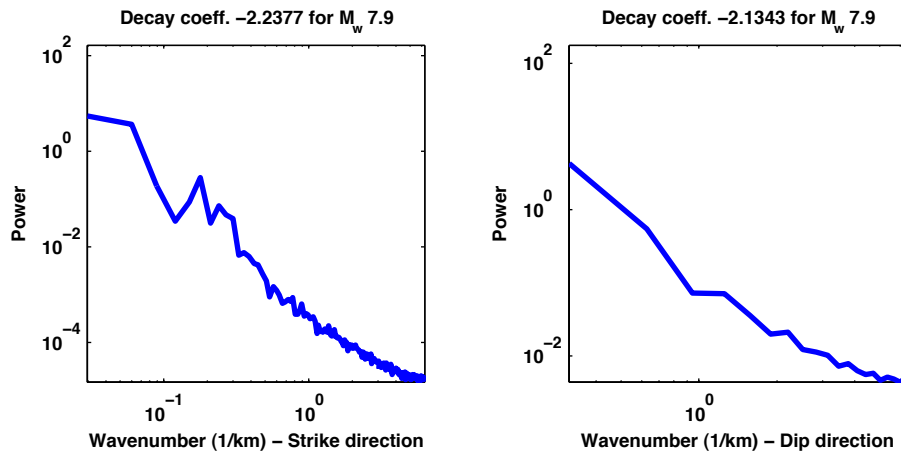


Figure 2.3. Power spectral density (PSD) of the slip shown in Fig. 2.2. along strike (left) and along dip (right).

2.2. Rupture-speed (V_r)

Laboratory earthquakes (Lu et al. 2010) show the influence of initial fault shear stress on rupture speed. Initial shear stress, in case of a strike-slip fault, can be determined using the orientation (θ) between maximum principal stress (σ_1) and fault strike. Evaluating θ along the fault forms an important step in estimating the initial shear stress (τ) and in further determining the rupture speed distribution for a source model.

2.2.1 Calculating θ the stresses acting on the fault

The World Stress Map (WSM) project (<http://www.world-stress-map.org>) compiles the azimuth of maximum principal stress (θ_a) at various near-fault locations, along with an estimate of measurement error (e_q) depending upon the quality of data. To account for this error, we add a random error to the reported estimate (θ_a^r) of θ_a as:

$$\theta_a = \theta_a^r \pm |0 \leq \text{random number} \leq 1| e_q \quad (2.2)$$

Finally, the orientation of σ_1 relative to the fault can be written as:

$$\theta = 180^\circ - |\phi - \theta_a| \quad (2.3)$$

where ϕ is the strike at the closest point on the fault. These near-fault data locations are coalesced into clusters based on their spatial distribution. We assume θ at each cluster location to be characterized by a lognormal distribution with mean equal to the arithmetic mean of θ for all the locations within the cluster and standard deviation calculated from the cluster with the highest number of WSM data points. We further assume that θ is constant along the depth of the fault i.e. rupture speed varies along fault length alone. All the sub-events on the fault that lie in the zone tributary to a data cluster are assigned randomized θ s drawn from the corresponding lognormal distribution. Within each of these tributary zones, θ is assumed to be constant for all sub-events over a distance less than or equal to the seismogenic depth “d” i.e., the same randomly generated θ is assigned to all these sub-events. Initial shear stress (τ) on the sub-event is then calculated using Eqns. 2.4. & 2.5., assuming ambient stresses in the crust adjacent to the fault are maintained by the frictional stability of small, high-friction fractures, and that fluid pressures in the crust are hydrostatic (Townend and Zoback 2000).

$$\bar{\sigma} = \frac{\sigma_1 + \sigma_3}{2} \simeq \rho_r g z; \quad p = \rho_w g z; \quad \Delta\sigma = \frac{2\mu_p(\bar{\sigma} - p)}{\sqrt{\mu_p^2 + 1}} \quad (2.4)$$

$$\tau = \frac{\Delta\sigma}{2} \sin 2\theta; \quad \sigma_n = \bar{\sigma} - p - \frac{\Delta\sigma}{2} \cos 2\theta \quad (2.5)$$

where p is the hydrostatic pressure, $\bar{\sigma}$ & $\Delta\sigma$ are the mean and differential stress, respectively, ρ_r & ρ_w are the density of rock and water, respectively, τ & σ_n are the initial shear and normal stress acting on the sub-event, and, g is the acceleration due to gravity. In our algorithm, z corresponds to half the seismogenic depth and μ_p ($= 0.6$) is the static friction coefficient for rock satisfying Coulomb frictional failure criterion.

2.2.2 Assigning rupture speeds

Loading factor (S) at the location of a given sub-event on the fault is calculated as:

$$\tau_p = \mu_p \sigma_n; \quad \tau_r = \mu_r \sigma_n \quad (2.6)$$

$$S = \frac{\tau_p - \tau_r}{\tau - \tau_r} \quad (2.7)$$

where μ_p ($=0.6$) & μ_r ($=0.1$) are the static and dynamic friction coefficients, respectively, and, τ_p & τ_r are the static and dynamic friction strength of the segment, respectively. If $S \geq 1.77$, rupture is assumed to propagate at sub-Rayleigh speeds (Andrews 1976) and a rupture speed of $0.87V_s$ is assigned for all segments along depth at that location. If $S \leq 1.77$, it is assumed that stress conditions exist for rupture to transition to super-shear speeds and a critical crack length (L_c) and transition length (L_t) are calculated as (Rosakis et al. 2007):

$$L_c = \frac{G(\tau_p - \tau_r)d_0}{\pi(1-\nu)(\tau - \tau_r)^2}; \quad f(S) = 9.8(1.77 - S)^{-3} \quad (2.8)$$

$$L_t = L_c f(S) \quad (2.9)$$

where d_0 is a characteristic slip weakening distance chosen randomly from a uniform distribution between 0.5 & 1.0 (Ide and Takeo 1997), and ν ($=0.25$) is the Poisson ratio. If L_t is less than along length distance from hypocenter to the sub-event location, a local rupture speed of $1.67V_s$ along depth is assigned, else rupture speed is set as $0.87V_s$.

2.3. Slip Velocity-Time Function

We fit isosceles triangles to the slip velocity-time functions from a catalogue of pulse-like laboratory earthquakes using an L_1 norm (see Fig. 2.4.). We develop a lognormal distribution to characterize the

slip to rise-time ratios obtained from this minimization for all available laboratory earthquakes. For a given slip model, we generate a realization of slip to rise-time ratio using this distribution. Since fault slip is known within each sub-event, we can compute the rise-time and hence the slip velocity within each sub-event. If the maximum rise time in the model exceeds $T_{r,max}$, we discard this slip velocity distribution across the fault and generate a new realization for slip to rise-time ratio. $T_{r,max}$ is the maximum rise-time in finite-source inversions from past earthquakes approximated from Fig. 2.4. by:

$$0.5T_{r,max} = 1.5M_w - 8.3 \quad (2.10)$$

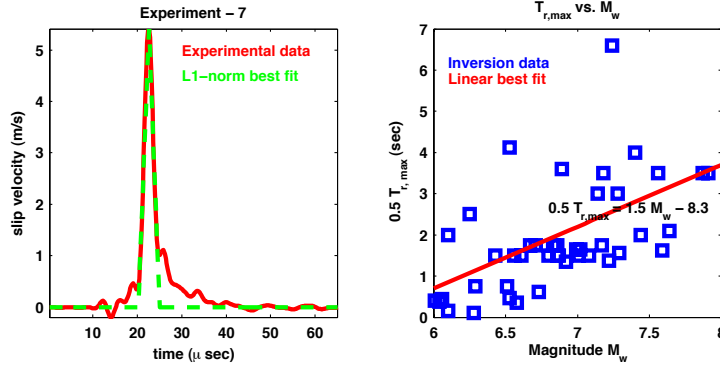


Figure 2.4. (left) Slip velocity plotted as a function of time for a laboratory earthquake; (right) Maximum rise time in source models plotted as a function of magnitude as found in finite-source inversions of past earthquakes.

3. APPLICATION TO THE SAN ANDREAS FAULT

Using the recursive division algorithm, we generate a suite of five stochastic source model realizations for a $M_w 7.9$ earthquake along the Southern San Andreas Fault. Each source realization is placed at 5 locations from Parkfield to Bombay Beach spaced uniformly along the fault and 10 rupture scenarios are generated using two rupture propagation directions (north-to-south and south-to-north; note that the slip distribution is also reversed). A total of 50 unilaterally propagating earthquakes (5 models x 5 locations x 2 directivities) are generated. Using SPECfEM3D (Komatitsch and Tromp 1999), an open source wave propagation package based on the spectral element method, 3-component waveforms are computed at 636 stations in Southern California for all the scenarios. The waveforms are low-pass filtered with a corner at 2 seconds [the underlying SCEC CVM-H wave speed model (Plesch et al. 2011) is capable of resolving waves with periods longer than 2s only]. To ensure that the source models generated by the recursive division algorithm are credible, we make statistical comparisons of

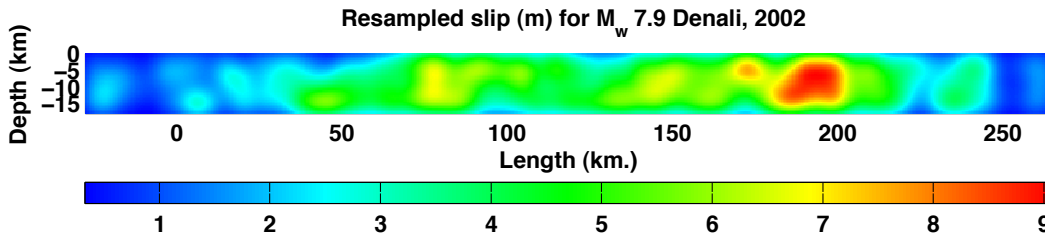


Figure 3.1. Slip model for 2002, $M_w 7.9$ Denali earthquake by Krishnan et al. (2006).

the peak ground velocities (PGV) generated by these models against the peak velocities generated by a finite-source inversion of an earthquake with equivalent magnitude. We chose a finite-source model of the 2002 $M_w 7.9$ Denali earthquake (see Fig. 3.1.) by Krishnan et al. (2006) for this exercise. We compute 3-component synthetics at the 636 Southern California sites for the 10 rupture scenarios (5 locations x 2 rupture directions) using this model as well. From the stochastic model set, we select the “median” model for the validation exercise as follows:

- i. For each stochastic source realization, we compute the median PGV for the two horizontal components of synthetic ground motion waveforms at the 636 sites from each of the 10 rupture scenarios (5 locations x 2 rupture directions).
- ii. We compute the median of the 10 values from (i) for each stochastic source realization. These are shown plotted as solid lines in Fig. 3.2. Simultaneously, we compute the median PGV from the combined suite of 50 earthquakes (10 rupture scenarios x 5 stochastic source models). This median ground motion is shown plotted as dashed lines in Fig. 3.2.
- iii. The source realization whose median PGV values are closest to the median PGV from (iii) is considered the “median” model and the stochastic features of the ground motions from this model are used in the validation exercise.

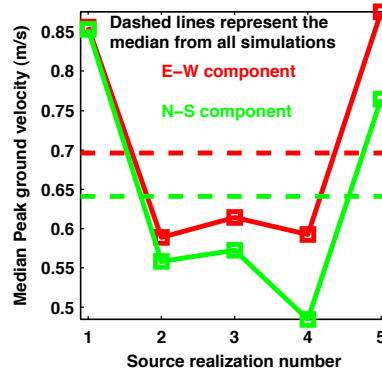


Figure 3.2. Median PGV for 10 rupture scenarios using each of the 5 stochastic source realizations compared against that from all 50 earthquakes. The earthquakes are of $M_w 7.9$ rupturing the San Andreas fault at 5 different locations. The synthetic ground motions are computed at 636 sites in Southern California.

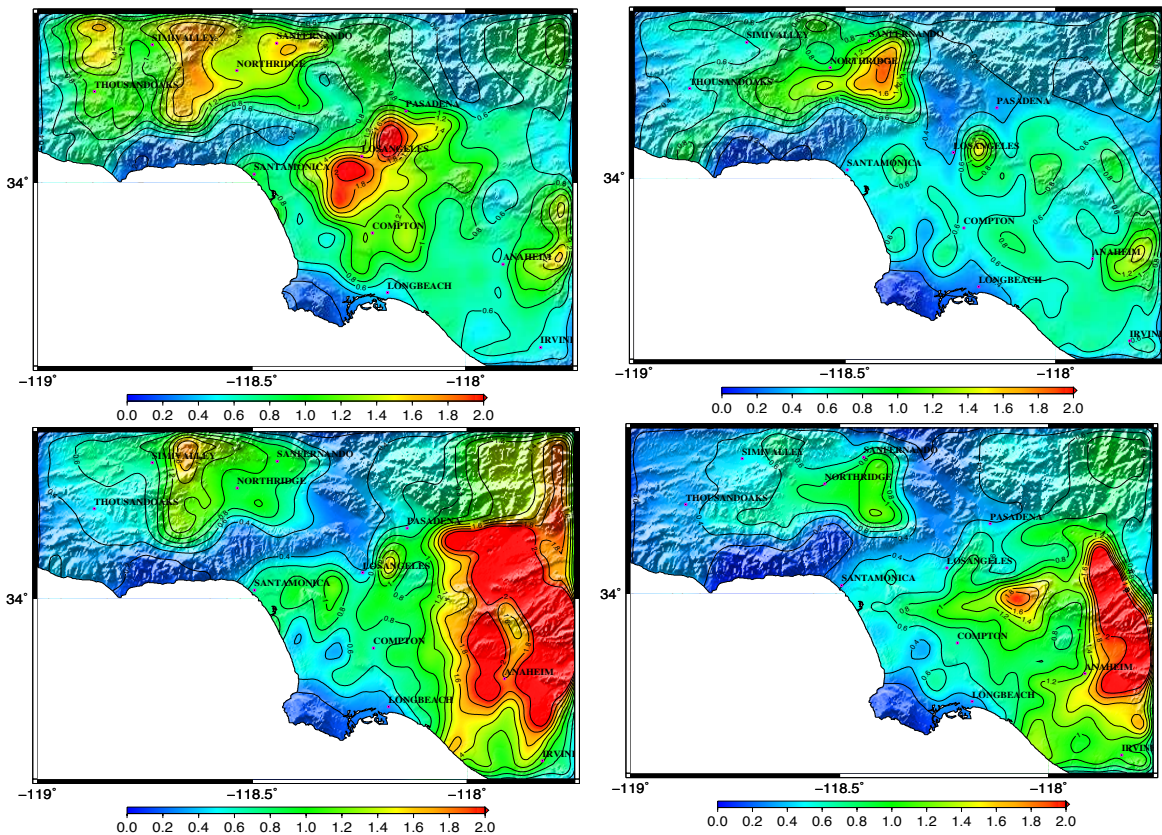


Figure 3.3. Peak ground velocity (m/s) maps of the (left) east-west and (right) north-south components for the (top) “median” model and (bottom) the Denali model located midway between Parkfield and Bombay Beach.

The peak ground velocity maps computed for location “3” (approximately mid-way between Parkfield and Bombay beach) using the “median” model (Fig. 2.2.) and the Denali model (Fig. 3.1.) are shown in Fig. 3.3. Since the large slip asperity in the Denali model is further southeast compared to the “median” model, the ground motions from the Denali model are far more intense in the San Gabriel Valley (which is further east) than in the Los Angeles Basin. However, the overall intensities of ground motion are not vastly different. This can be seen in the statistical comparisons shown in Fig. 3.4. Plotted there are the histograms of PGV from four of the five rupture locations for the “median” model and compared against that from the Denali model.

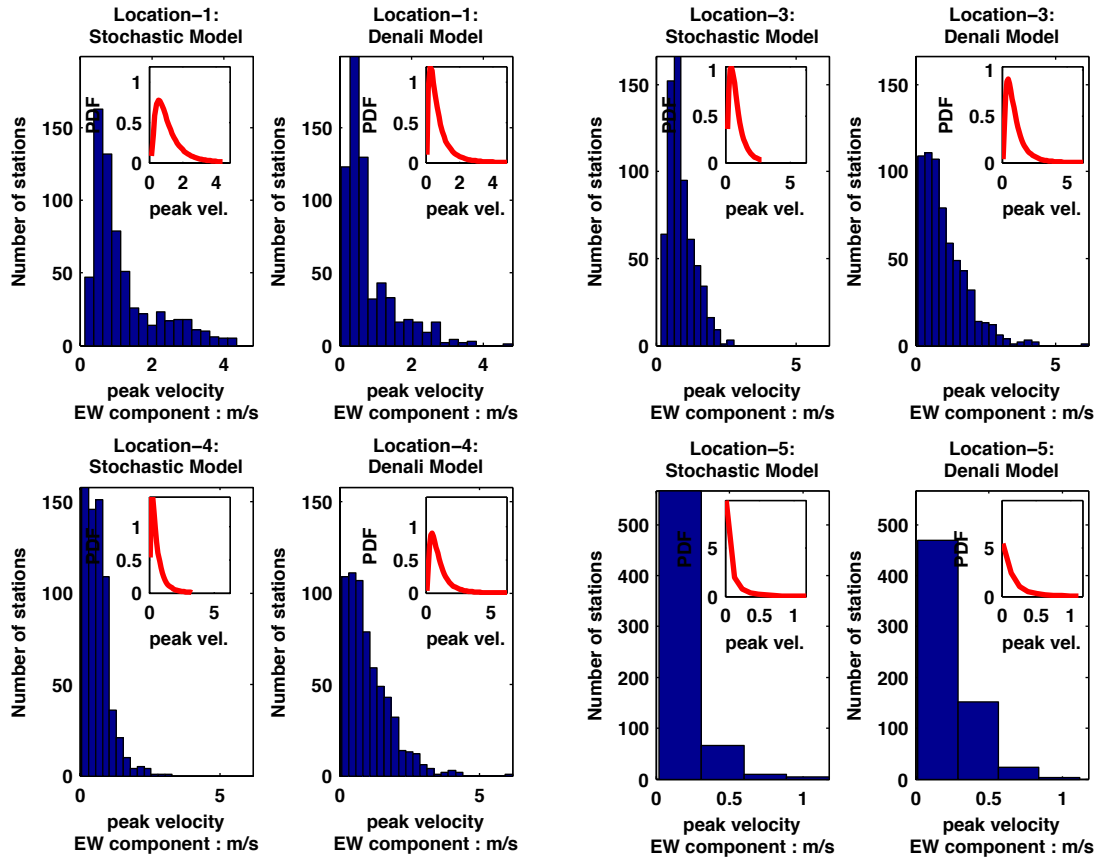


Figure 3.4. Histograms of peak ground velocities of east-west component at 636 stations in Southern California using the “median” source model and the Denali model, rupturing at 4 different locations between Parkfield and Bombay Beach, and propagating north-to-south. Insets show the corresponding lognormal distribution fits.

4. ONGOING WORK

Work is ongoing to use this source model generation algorithm to create stochastic source models for earthquake magnitudes in the range 6.0-8.0 on southern San Andreas Fault. The resulting synthetic waveforms from these models will be used in performing non-linear dynamic analysis of 18-storey moment frame and 40-storey dual frame buildings across 636 sites in Southern California thus paving way for a probabilistic seismic risk analysis.

ACKNOWLEDGEMENT

This work is funded in part by NSF: CMMI Award No. 0926962. We thank Thomas Heaton (Caltech), Jean Paul Ampuero (Caltech), Dimitri Komatitsch (University of Pau, France), Martin Mai (KAUST), Rob Graves (USGS), and Chen Ji (UCSB) for offering valuable insights into various aspects of source physics and seismic wave propagation.

REFERENCES

- Aagaard, B.T., R.W. Graves, D.P. Schwartz, D.A. Ponce, and R.W. Graymer (2010). Ground-Motion Modeling of Hayward Fault Scenario Earthquakes, Part I: Construction of the Suite of Scenarios. *Bulletin of the Seismological Society of America*. **100:6**, 2927-2944.
- Andrews, D. (1976). Rupture velocity of plane strain shear cracks. *Journal of Geophysical Research*. **81:32**, 5679-5687.
- Andrews D. and Barall M. (2011). Specifying initial stress for dynamic heterogeneous earthquake source models. *Bulletin of the Seismological Society of America*. **101:5**, 2408-2417.
- Bouchon, M., M. Toksoz, H. Karabulut, M. Bouin, M. Dietrich, M. Aktar, and M. Edie (2002). Space and time evolution of rupture and faulting during the 1999 Izmit (Turkey) earthquake. *Bulletin of the Seismological Society of America*. **92:1**, 256-266.
- Bouchon, M., and M. Vallée (2003). Observation of long supershear rupture during the magnitude 8.1 Kunlunshan earthquake. *Science*. **301:5634**, 824-826.
- Brune J. (1970). Tectonic Stress and Spectra of Seismic Shear Waves From Earthquakes. *Journal of Geophysical Research*. **75:26**, 4997-&.
- Fialko Y., D. Sandwell, M. Simons, and P. Rosen (2005). Three dimensional deformation caused by the Bam, Iran, earthquake and the origin of shallow slip deficit. *Nature*. **435:7040**, 295-299.
- Frankel, A. (2004). Rupture process of the M 7.9 Denali fault, Alaska, earthquake: Subevents, directivity, and scaling of high-frequency ground motions. *Bulletin of the Seismological Society of America*. **94:6B**, S234-S255.
- Guatteri M., P. Mai, and G. Beroza (2004). A pseudo-dynamic approximation to dynamic rupture models for strong ground motion prediction. *Bulletin of the Seismological Society of America*. **89:6**, 1484-1504.
- Heidbach O., M. Tingay, A. Barth, J. Reinecker, D. Kurfeß and B. Müller (2008). The world stress map database release 2008 doi:10.1594/gfz.wsm.rel2008.
- Ide S. and M. Takeo (1997). Determination of constitutive relations of fault slip based on seismic wave analysis. *Journal of Geophysical Research-Solid Earth*. **102:B**, 27379-27391.
- Ji C., D. Helmberger, and D. Wald (2004). A teleseismic study of the 2002 Denali, Alaska, earthquake and implications for rapid strong motion estimation. *Earthquake Spectra*. **20:3**, 617-637.
- Komatitsch D. and J. Tromp (1999). Introduction to the spectral element method for three dimensional seismic wave propagation. *Geophysical Journal International*. **139:3**, 806-822.
- Krishnan, S., C. Ji, D. Komatitsch, and J. Tromp (2006). Case studies of Damage to Tall Steel Moment-Frame Buildings in Southern California During Large San Andreas Earthquakes. *Bulletin of the Seismological Society of America*. **96:4**, 1523-1537.
- Liu P., R.J. Archuleta, and S.H. Hartzell (2006). Prediction of Broadband Ground-Motion Time Histories: Hybrid Low/High-Frequency Method with Correlated Random Source Parameters. *Bulletin of the Seismological Society of America*. **96:6**, 2118-2130.
- Lu X., A.J. Rosakis and N. Lapusta (2010). Rupture modes in laboratory earthquakes: Effect of fault prestress and nucleation conditions. *Journal of Geophysical Research*. **115:B12**.
- Mai P. and G. Beroza (2002). A spatial random field model to characterize complexity in earthquake slip. *Journal of Geophysical Research*. **107:1029**, 2001.
- Plesch, A., C. Tape, J.R. Graves, P. Small, G. Ely and J.H. Shaw (2011). Updates for the CVM-H including new representations of the offshore Santa Maria and San Bernardino basin and a new Moho surface. *2011 Southern California Earthquake Center Annual Meeting, Proceedings and Abstracts*. **21**.
- Rosakis A., K. Xia, G. Lykotrakis, and H. Kanamori (2007). Dynamic shear rupture in frictional interfaces: speeds, directionality and modes. *Treatise in geophysics, Elsevier, Amsterdam*. **4:-**, 153-192.
- Schmedes J., R.J. Archuleta, and D. Lavallée (2010). Correlation of earthquake source parameters inferred from dynamic rupture simulations. *Journal of Geophysical Research*. **115:-**, B03304.
- Somerville P., K. Irikura, R. Graves, S. Sawada, D. Wald, N. Abrahamson, Y. Iwasaki, T. Kagawa, N. Smith, and A. Kowada (1999). Characterizing Earthquake Rupture Models for the Prediction of Strong Ground Motion. *Seismological Research Letters*, **70**, 59-80.
- Townend J. and M. Zoback (2000). How faulting keeps the crust strong. *Geology*. **28:5**, 399.